ORIGINAL ARTICLE

A highly crystalline face-on π-conjugated polymer based on alkoxythiophene-flanked benzobisthiazole for organic photovoltaics

Shuhei Doi[1] · Tsubasa Mikie[1] · Kodai Yamanaka[1] · Yuki Sato[2] · Hideo Ohkita[2] · Masahiko Saito[1] · Itaru Osaka[1]

Abstract

The use of noncovalent intramolecular interactions constitutes a powerful design strategy for preparing π-conjugated polymers featuring high backbone coplanarities and thereby high crystallinities. Herein, we report the design and synthesis of an alkoxythiophene-flanked benzobisthiazole (BBTz) as a new building unit for π-conjugated polymers, which was subsequently copolymerized to give a simple BBTz-bithiophene copolymer with alkyl and alkoxy groups (**PDBTz2**). Owing to the S···O noncovalent intramolecular interactions between the alkoxy oxygens and thiazole sulfurs in BBTz, **PDBTz2** showed greater coplanarity and crystallinity than its alkyl counterpart, **PDBTz1**. Interestingly, the backbone orientation was completely altered from the edge-on orientation observed for **PDBTz1** to a face-on orientation for **PDBTz2**, which is preferable for organic photovoltaics (OPVs). In addition, the electron-donating nature of the alkoxy group increased the HOMO energy level of **PDBTz2** compared to that of **PDBTz1**, which enabled photoinduced hole transfer from a nonfullerene acceptor, Y6, to the polymer. As a result, the short-circuit current density of an organic photovoltaic cell based on **PDBTz2** and Y6 was significantly greater than that of a cell based on **PDBTz1** and Y6. This study confirmed that alkoxythiophene-flanked BBTz is a promising building unit for high-performance π-conjugated polymers.

Introduction

Solution-processable organic photovoltaics (OPVs) constitute an important next-generation photovoltaic technology featuring flexibility, light weight, and semitransparency [1–3]. Recent progress in the use of π-conjugated materials and polymers as donors and acceptors, particularly small-bandgap nonfullerene acceptors (NFAs), has dramatically improved power conversion efficiencies (PCEs) [4–6]. For π-conjugated polymer donors, a promising molecular design strategy involves extension of the π-electron system of the building unit [7, 8]. For example, most of the high-performance polymers reported recently incorporate benzo[1,2-*b*:4,5-*b'*]dithiophene (BDT), a relatively electron-rich building unit, in their polymer backbones [9–11]. Additionally, π-extensions of electron-deficient heteroaromatic cobuilding units have also been studied [12]. Among a number of electron-deficient heteroaromatic systems, thiazole-based fused rings such as thiazolo[5,4-*d*]thiazole (TzTz) and benzo[1,2-*d*:4,5-*d'*]bisthiazole (BBTz) have been shown to be excellent systems for building π-conjugated polymers (Fig. 1a, b) [13–15]. Indeed, π-conjugated polymers consisting of BDT and alkylthiophene-flanked TzTz or BBTz showed relatively high PCEs in NFA-based cells [16–22].

The use of noncovalent intramolecular interactions to enable coplanarity of the polymer backbone is also an important molecular design strategy for the development of high-performance π-conjugated polymers [23]. The fluorine atom is a common substituent that interacts with hydrogen and sulfur atoms; thus, fluorine is often introduced on heteroaromatic rings linked with thiophenes or thiazoles
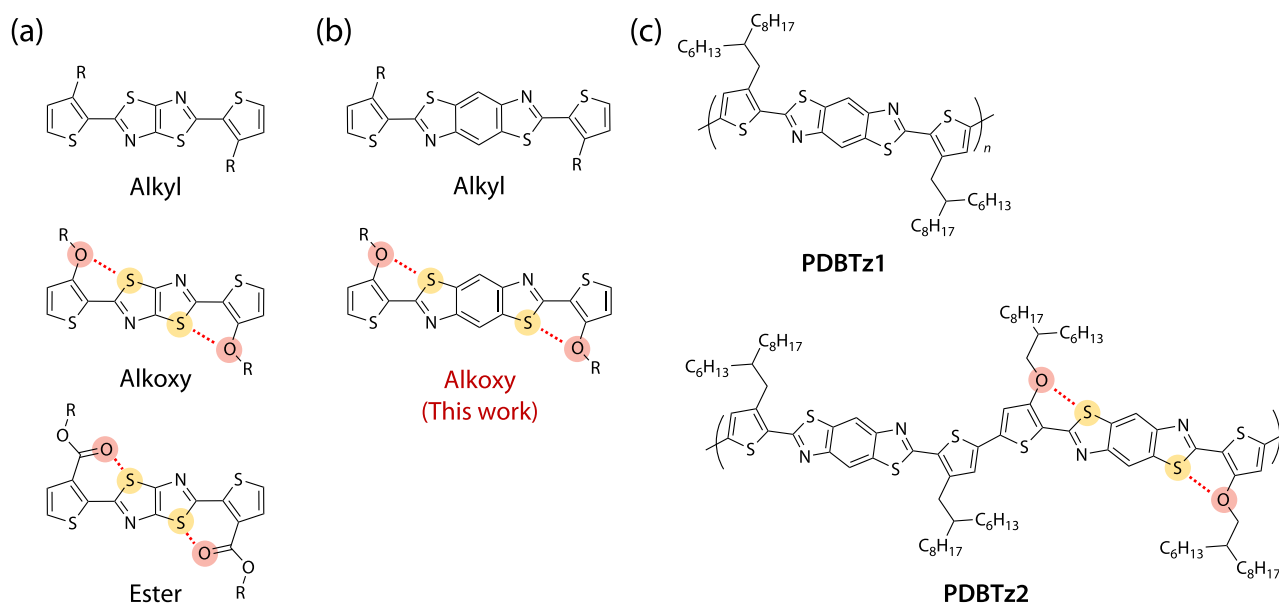
Fig. 1 Chemical structures of (**a**) thiophene-TzTz-thiophene and (**b**) thiophene-BBTz-thiophene building units with alkyl, alkoxy, and ester groups, and (**c**) BBTz-based polymers, **PDBTz1** and **PDBTz2**

[24–26]. The oxygen atom can also interact with the sulfur atom; thus, alkoxy and ester groups are often used as side chains instead of alkyl groups on heteroaromatic rings linked with thiophene or thiazole [27, 28]. For example, our group reported the use of alkoxythiophene- and esterthiophene-flanked TzTz as building blocks for π-conjugated polymers, which were more crystalline than their alkyl counterparts (Fig. 1a) [29, 30]. As a lower highest occupied molecular orbital (HOMO) energy level is preferred for donor materials to provide high open-circuit voltage (V_{OC}) in OPV [31], electron-withdrawing ester groups are typically chosen for the side chains rather than electron-donating alkoxy groups. However, for polymers with inherent very low HOMO energy levels, the alkoxy group functions better than the ester group. Herein, we synthesized alkoxythiophene-flanked BBTz as a novel building unit (Fig. 1b) and two simple BBTz-based polymers incorporating bithiophene counits, i.e., **PDBTz1**, which has alkyl groups on all of the bithiophene units, and **PDBTz2**, which has alternating alkyl and alkoxy groups on the bithiophene units (Fig. 1c). Notably, when the polymers were blended with Y6, a benchmark NFA, hole transfer was inefficient in the **PDBTz1**:Y6 blend because the offset energy of the HOMOs was too small, hole transfer was significantly improved in the **PDBTz2**:Y6 blend due to the sufficiently large offset originating from the elevated HOMO energy level in **PDBTz2**. Interestingly, whereas **PDBTz1** exhibited a highly crystalline structure with nearly complete edge-on orientations, **PDBTz2** exhibited a highly crystalline structure with nearly complete face-on orientations, which resulted in greater out-of-plane charge

transport in **PDBTz2** than in **PDBTz1**. As a result, **PDBTz2** showed greater photovoltaic performance than **PDBTz1**.

Syntheses

The synthetic routes to the BBTz-bithiophene copolymers are shown in Scheme 1. The ring-closing reaction of 2,5-diaminobenzene-1,4-dithiol dihydrochloride (**1**) and 3-(2-hexyldecyl)thiophene-2-aldehyde (**2**) afforded an alkylthiophene-flanked BBTz derivative (**3**) in 35% yield [32]. Subsequently, **3** was dibrominated with *N*-bromo-succinimide (NBS) in a chloroform (CF)/acetic acid (AcOH) cosolvent system to give the dibrominated BBTz monomer (**4**) in 80% yield. **4** was then distannylated via lithiation with *n*-butyl lithium and subsequent treatment with trimethyltin chloride to provide **5** in 76% yield. An alkoxythiophene-flanked BBTz derivative (**7**) was obtained in 15% yield via a ring-closing reaction using **1** and 3-(2-hexyldecyloxy)thiophene-2-carbaldehyde (**6**) and then was dibrominated to give **8** in 75% yield. **4** was copolymerized with **5** and **8** to afford **PDBTz1** and **PDBTz2**, respectively, via the Stille coupling reaction with Pd$_2$(dba)$_3$·CHCl$_3$ and P(*o*-tol)$_3$ as the catalyst system. The molecular weights of the polymers were determined with high-temperature gel permeation chromatography (GPC) with trichlorobenzene (TCB) as the eluent at 180 °C. The number-average molecular weight (M_n) and dispersity (Đ) were 36,200 and 1.9 for **PDBTz1** and 33,500 and 2.3 for **PDBTz2**, respectively (Fig. S1). Interestingly, both polymers were soluble in CF
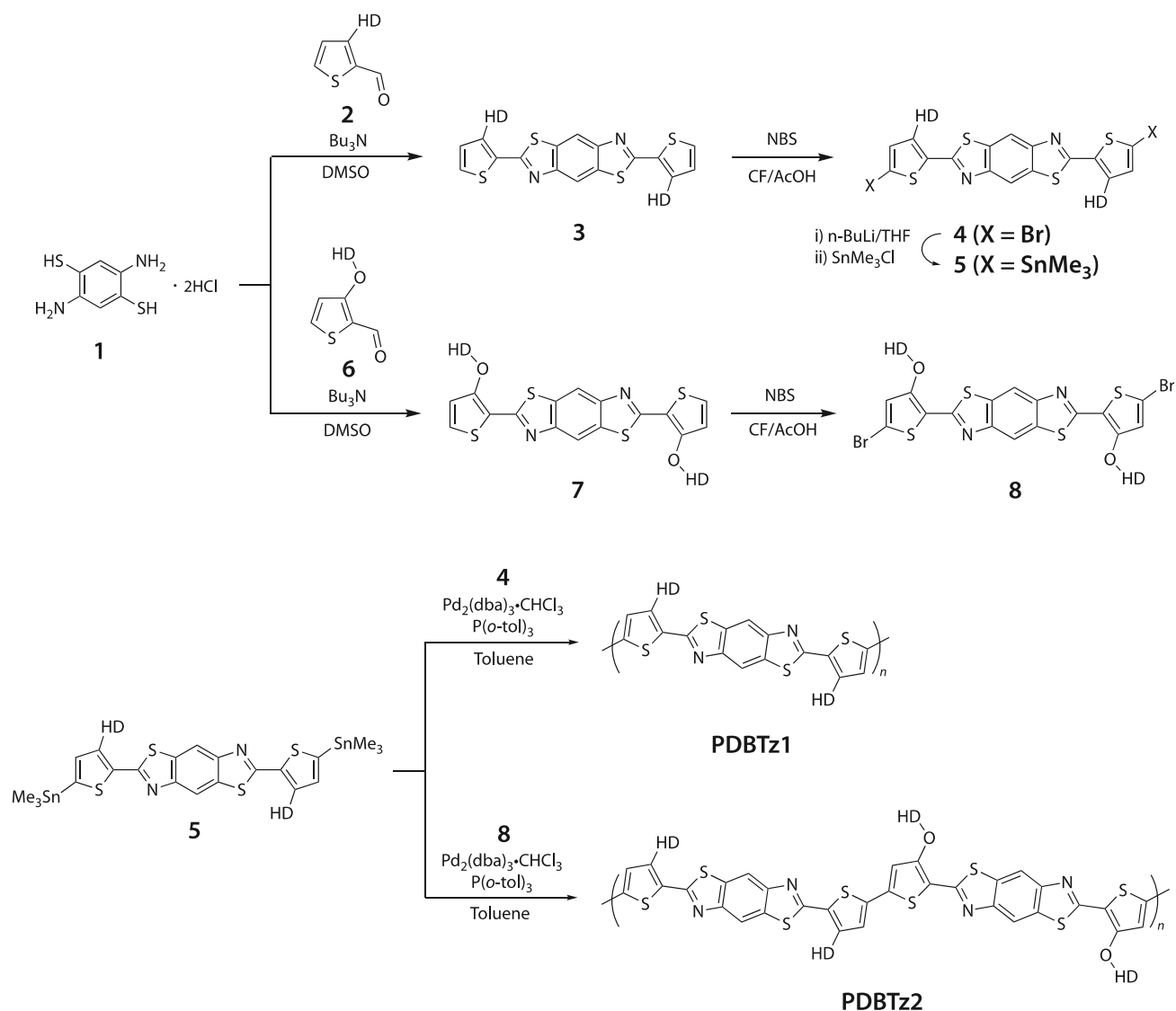
Scheme 1 Synthetic route to BBTz-based polymers with alkyl groups (**PDBTz1**) and alkoxy groups (**PDBTz2**). HD = 2-hexyldecyl

and CB even at room temperature, even though BBTz had a π-extended building unit without substituents. Differential scanning calorimetry showed no phase transitions below 350 °C (Fig. S2), indicating that both polymers had good thermal stabilities.

Polymer properties

Cyclic voltammetry (CV) was used to evaluate the energy levels of the polymers. Figure 2a shows the cyclic voltammograms of the polymers. The HOMO and LUMO energy levels (E_{HOMO} and E_{LUMO}, respectively) were determined from the onset redox potentials, which were −1.99 and 0.84 V for **PDBTz1** and −1.97 and 0.67 V for **PDBTz2**, respectively, after calibration with ferrocene. The

energy levels of the polymers, along with those of Y6, a benchmark NFA, are summarized in Fig. 2b and Table 1. The E_{HOMO} of **PDBTz2** was −5.47 eV, which was 0.17 eV greater than that of **PDBTz1** (−5.64 eV). In addition, photoemission yield spectroscopy (PYS) indicated that **PDBTz2** had a higher E_{HOMO} (−5.01 eV) than **PDBTz1** (−5.28 eV) by 0.27 eV (Fig. S3). The higher HOMO energy level of **PDBTz2** was explained by the stronger electron-donating nature of the alkoxy group relative to that of the alkyl group. As a result, the HOMO energy offset between the polymer and Y6 was 0.22 eV for **PDBTz2**, which was larger than that for **PDBTz1** (0.05 eV). On the other hand, both polymers had similar LUMO energy levels of approximately −2.80 eV, which was likely dependent on the electron-deficient BBTz unit. Thus, **PDBTz2** is expected to have a smaller bandgap than **PDBTz1**. These trends
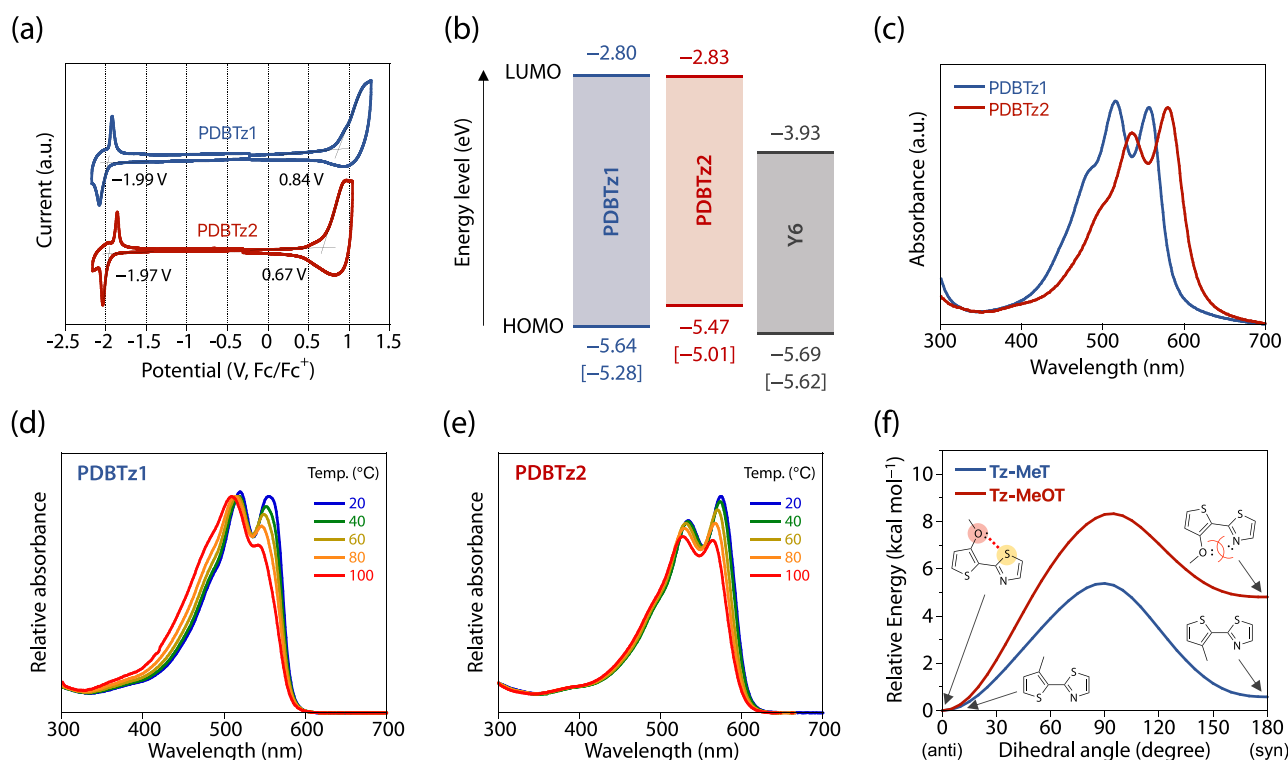
Fig. 2 **a** Cyclic voltammograms of the polymers in the thin films. **b** Energy diagrams of the polymers along with Y6. The value in brackets is the E_{HOMO} determined by the PYS measurement. **c** UV–vis absorption spectra of the polymers in thin films. Temperature-dependent UV–vis absorption spectra of (**d**) **PDBTz1** and (**e**) **PDBTz2** in CB solution. **f** Energy variations of the thiazole–methylthiophene (Tz–MeT) and thiazole–methoxythiophene (Tz–MeOT) linkages as a function of dihedral angle calculated with the DFT method (B3LYP/6-31G(d) level)

Table 1 Optical properties of the polymers

Polymer	E_{HOMO} (eV)[a]	E_{LUMO} (eV)[c]	λ_{max} (nm)	λ_{edge} (nm)	E_g^{opt} (eV)[d]
PDBTz1	−5.64 [−5.28][b]	−2.81	515, 557	589	2.11
PDBTz2	−5.47 [−5.01][b]	−2.83	536, 580	616	2.01

[a]Estimated with $E_{HOMO} = -4.80 - E_{ox}^{onset}$

[b]The E_{HOMO} determined by PYS measurement

[c]Estimated with $E_{LUMO} = -4.80 - E_{red}^{onset}$

[d]Optical bandgap determined from the absorption onset

were roughly consistent with the results from DFT calculations at the B3LYP 6-31G(d) level (Fig. S4).

The UV–vis spectra of the polymer thin films are shown in Fig. 2c, and the corresponding optical parameters are listed in Table 1. **PDBTz1** exhibited two absorption maxima (λ_{max}) at 557 and 515 nm, which correspond to the 0–0 and 0–1 transitions, respectively. **PDBTz2** also had λ_{max} values of 580 and 536 nm, which were ~20 nm greater than those of **PDBTz1**. The optical bandgap (E_g^{opt}) for **PDBTz2** calculated with the absorption onset (λ_{onset}) was 2.01 eV ($\lambda_{onset} = 616$ nm), which was smaller than that for **PDBTz1** ($E_g^{opt} = 2.11$ eV, $\lambda_{onset} = 589$ nm). Interestingly, the intensity ratio of the 0–0 band with respect to the 0–1 band (I_{0-0}/I_{0-1}) was greater in **PDBTz2** (1.13) than in **PDBTz1** (0.97). We also noted that **PDBTz2** had a significantly greater

absorption coefficient than **PDBTz1** in both the solution and thin films (Fig. S5 and Table S2), which was consistent with the computations (Fig. S6). These results implied that the polymer backbone in **PDBTz2** was more coplanar and rigid than that in **PDBTz1** [33, 34].

We also measured the temperature-dependent UV–vis absorption spectra of the polymers in the CB solution (Fig. 2d, e). However, in **PDBTz1**, the intensity of the 0–0 band was significantly lower than that of the 0–1 band at 100 °C, whereas in **PDBTz2**, the intensity of the 0–0 band was still similar to that of the 0–1 band. This suggested that **PDBTz2** has a more rigid backbone and greater aggregation than **PDBTz1**. This was validated by plotting the energy as a function of the dihedral angle for the thiazole–methylthiophene (Tz–MeT) and thiazole–methoxythiophene (Tz-MeOT)

linkages, as models for **PDBTz1** and **PDBTz2**; these were calculated with the DFT method (B3LYP/6-31G(d) level) (Fig. 2f). The torsional energy barrier, the difference between the energy at a dihedral angle of 90° and that at 0°, for Tz–MeOT was 8.3 kcal mol^{-1}, which was ~1.5 times greater than that for Tz–MeT (5.4 kcal mol^{-1}). This suggested that Tz–MeOT suppressed torsion more than Tz–MeT, which was due to the S···O noncovalent intramolecular interactions between the sulfur atom in the thiazole ring and the oxygen in the alkoxy group. Therefore, it is expected that the backbone of **PDBTz2** is more coplanar than that of **PDBTz1**. Moreover, Tz–MeOT adopts the *anti*-conformation (a dihedral angle of 0°) rather than the *syn*-conformation (a dihedral angle of 180°) more readily than Tz–MeT, as the energy difference between these conformations was 4.8 kcal mol^{-1} for the former and 0.6 kcal mol^{-1} for the latter, which was likely due to the N···O Coulombic repulsion between the lone pairs on nitrogen in the thiazole and the methoxy oxygen. Therefore, **PDBTz2** should predominantly exhibit an *anti*-conformation and provide a more regular backbone structure than **PDBTz1**, which would increase the backbone order and crystallinity.

Photovoltaic characteristics

We fabricated OPV cells with conventional structures (ITO/ PEDOT:PSS/polymer:Y6/PNDIT-F3N-Br/Ag). A polymer:Y6 blend with a weight ratio of 1:1.2 was spin-coated with a 6.0 g L^{-1} CF solution containing 0.5% (v/v) 1-chloronaphthalene. Figures 3a, b show the current density–voltage (*J–V*) curves and external quantum efficiency (EQE) spectra of the cells, and the photovoltaic parameters are listed in Table 2. The **PDBTz2** cell showed a short-circuit current density (J_{SC}) of 26.0 mA cm^{-2}, which was approximately twice that of the **PDBTz1** cell (12.8 mA cm^{-2}). Correspondingly, the maximum EQE of the **PDBTz2** cell (85%) was also approximately twice that of the **PDBTz1** cell (42%). The J_{SC} value calculated from the EQE spectra (J_{SC}^{EQE}) was consistent with the J_{SC} value obtained from the *J–V* measurements (Table 2). The **PDBTz2** cell exhibited a lower V_{OC} (0.73 V) than the **PDBTz1** cell (0.77 V), which was consistent with the higher E_{HOMO} of **PDBTz2** relative to that of **PDBTz1**. The fill factors (FF) were relatively low for both cells: it was 0.47 for **PDBTz2** and 0.49 for **PDBTz1**. As a result, the **PDBTz2** cell showed a PCE of 8.8%, which was much greater than that of the **PDBTz1** cell (4.6%).

We also tested OPV cells with inverted structures (ITO/ ZnO/polymer:Y6/MoO$_x$/Ag), in which the blended films were fabricated similar to those of conventional cells. For **PDBTz2**, the inverted cell provided a lower J_{SC} (22.7 mA cm^{-2}) but a higher V_{OC} (0.79 V) and FF (0.61) than the conventional cells, leading to higher PCEs of up to 10.9%. This PCE was also higher than that of the inverted cell for **PDBTz1** (PCE = 3.8%, J_{SC} = 9.4 mA cm^{-2}, V_{OC} = 0.80 V, FF = 0.50).
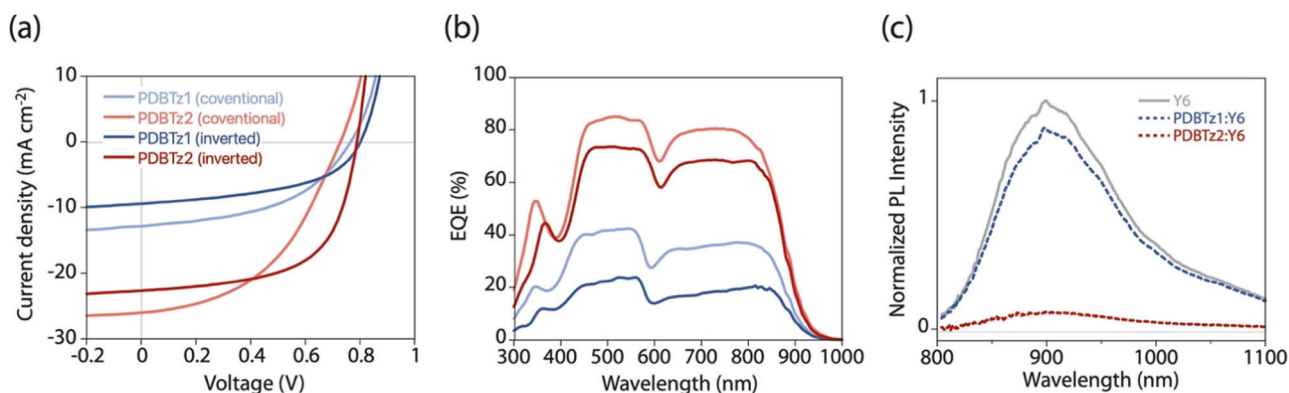

Fig. 3 **a** *J–V* curves and (**b**) EQE spectra of the polymer:Y6 cells. **c** Photoluminescence spectra of the Y6 neat film and polymer:Y6 blended films excited at 680 nm (Y6 excitation). **c** Photoluminescence spectra for a Y6 neat film and polymer:Y6 blend films excited at 680 nm (Y6 excitation)

Table 2 Photovoltaic properties of the polymer:Y6 cells

Polymer	Device structure	J_{SC} [J_{SC}^{EQE}] (mA cm^{-2})[a]	V_{OC} (V)	FF	PCE$_{max\ [ave.]}$[b] (%)
PDBTz1	Conventional	12.2 [11.6]	0.77	0.49	4.6 [4.1]
	Inverted	9.4 [9.1]	0.80	0.50	3.8 [3.6]
PDBTz2	Conventional	26.0 [24.6]	0.73	0.47	8.8 [8.1]
	Inverted	22.7 [21.4]	0.79	0.61	10.9 [9.4]

[a]The value in bracket is the calculated J_{sc} from EQE spectra

[b]The value in bracket is the average PCE of 10 devices

To understand the significant difference in the J_{SC} values for the **PDBTz1** cell and the **PDBTz2** cell, we investigated the photoluminescence (PL) quenching efficiencies of the blended films (Fig. 3c). When excited at 560 nm (polymer excitation), the quenching efficiencies were nearly 100% for both the **PDBTz1**:Y6 and **PDBTz2**:Y6 blended films. Quenching of the polymer PL was likely dominated by energy transfer (Fig. S7). In contrast, when excited at 680 nm (Y6 excitation), the quenching efficiency was 12% for the **PDBTz1**:Y6 blend film and 92% for the **PDBTz2**:Y6 blend film. This indicated that, whereas hole transfer from Y6 to **PDBTz1** was inefficient, hole transfer from Y6 to **PDBTz2** was highly efficient. Because there were no significant differences in the morphologies of the two films (Fig. S8), the inefficient hole transfer of the **PDBTz1**:Y6 blended film was ascribed to the small energy offset between the E_{HOMOS}, which accounted for the low J_{SC} in the **PDBTz1** cell.

Packing orders of the polymers

Grazing-incidence X-ray diffraction (GIXD) measurements were performed to investigate the packing orders of the

polymers. Figure 4a–d depicts the two-dimensional (2D) GIXD patterns and cross-sectional diffraction profiles (Fig. 4e, f) of the neat and blended polymer films. The diffraction parameters of the neat and blended polymer films are listed in Table 3. In the neat films (Fig. 4a, b), **PDBTz1** adopted an edge-on orientation, as the (0 1 0) π–π stacking diffraction ($q_{xy} \approx 1.70$ Å^{-1}) and (h 0 0) lamellar diffractions ($\sim q_z \approx 0.33$ Å^{-1}) appeared along the q_{xy} and $\sim q_z$ axes, respectively. Moreover, **PDBTz2** adopted a face-on orientation, as the (0 1 0) π–π stacking diffraction peak ($\sim q_z \approx 1.75$ Å^{-1}) and (h 0 0) lamellar diffraction peak ($q_{xy} \approx 0.29$ Å^{-1}) appeared along the $\sim q_z$ and q_{xy} axes, respectively (Fig. 4e). The π–π stacking distance (d_π) of **PDBTz2** was 3.55 Å, which was significantly shorter than that of **PDBTz1** (3.69 Å). Although the coherence length of the π–π stacking diffraction (CL_π) for **PDBTz2** (31.9 Å) was slightly smaller than that for **PDBTz1** (37.7 Å), the values should not be directly compared because these diffraction angles appeared in the wide-angle region of the different q axes. Both polymers exhibited higher-order lamellar diffractions, up to the fourth order, which indicated their highly crystalline natures. Notably, such higher-order lamellar diffractions are rarely observed for polymers with face-on orientations because highly crystalline polymers
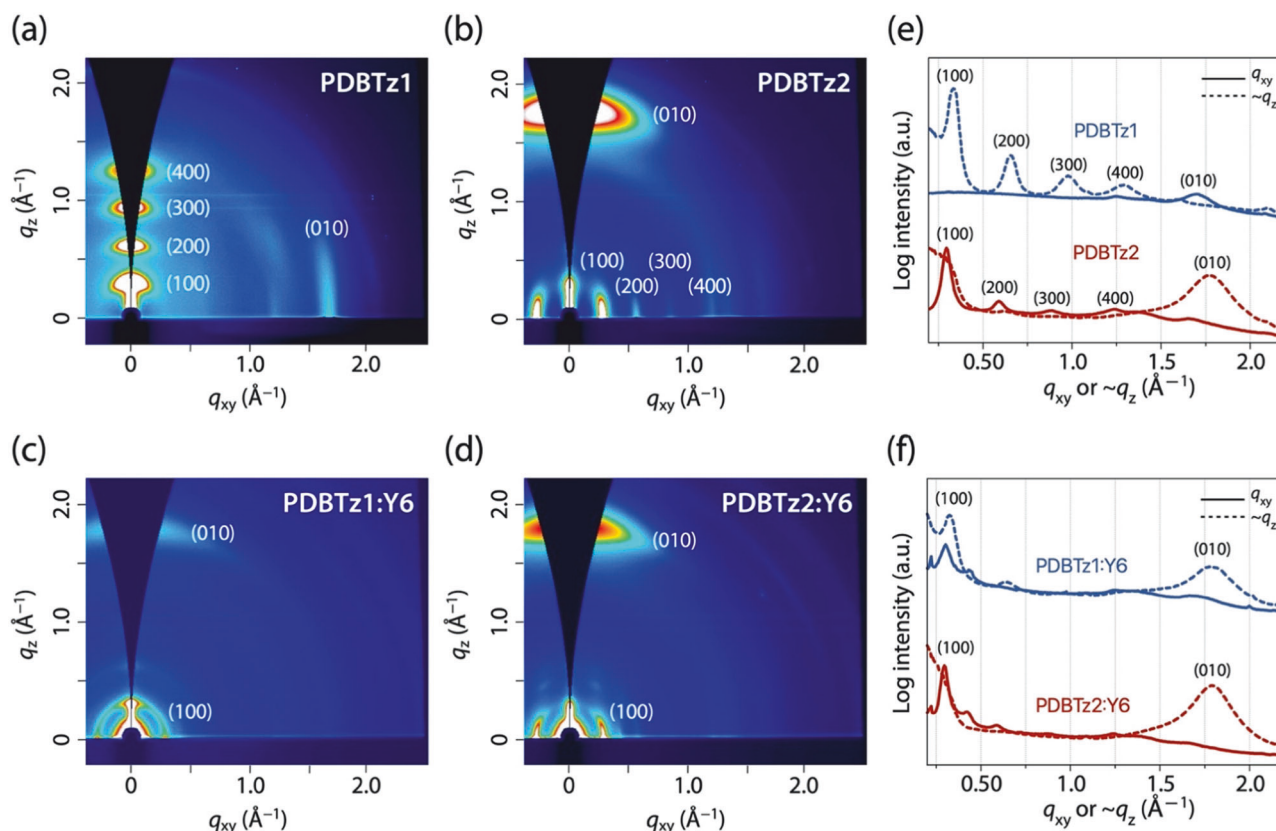

Fig. 4 a–d 2D GIXD patterns of the polymer neat films and polymer:Y6 blended films. **a PDBTz1**, **b PDBTz2**, **c PDBTz1**:Y6, and **d PDBTz2**:Y6. **e, f** Cross-sectional diffraction profiles cut from the 2D GIXD patterns along the q_{xy} (solid line) and $\sim q_z$ (dashed line) axes. **e** Polymer neat films. **f** Polymer:Y6 blended films

Table 3 Structural parameters extracted from the GIXD measurement parameters of the polymer neat films and polymer:Y6 blend films

Film	(0 1 0) π–π stacking		(1 0 0) lamellar	
	d_π (Å)	CL_π (Å)[a]	d_L (Å)	CL_L (Å)[a]
PDBTz1	3.69	37.7	18.9	138
PDBTz2	3.55	31.9	21.3	164
PDBTz1:Y6	3.51	26.0	19.2	51
PDBTz2:Y6	3.51	31.4	21.2	146

[a]The coherence length for the π–π stacking (CL_π) and lamellar structure (CL_L), which were estimated from the simplified Scherrer's equation, $L_C = 2\pi/\text{fwhm}$, where fwhm is the full-width at half-maximum

typically exhibit edge-on orientations [35]. The lamellar distance (d_L) of **PDBTz2** (21.3 Å) was greater than that of **PDBTz1** (18.8 Å). This difference was attributed to the 2-hexyldecyloxy group in **PDBTz2**, which were longer than the 2-hexyldecyl groups in **PDBTz1**. The coherence length corresponding to the (1 0 0) lamellar structure (CL_L) was 164 Å for **PDBTz2**, which was significantly greater than that of **PDBTz1** (138 Å). Overall, we concluded that **PDBTz2** was more crystalline than **PDBTz1**, which was attributed to the greater backbone coplanarity of **PDBTz2**.

The polymer:Y6 blend films exhibited clear diffraction along the $\sim q_z$ axis corresponding to the (0 1 0) π–π stacking structures with a d_π of 3.51 Å (Fig. 4c, d, f). The CL_π for the **PDBTz2**:Y6 blended film was 31.4 Å, which was larger than that of the **PDBTz1**:Y6 blended film (26.0 Å). However, as the diffraction angles from the (0 1 0) π–π stacked structures of the polymer and Y6 should overlap, we could not fairly compare the crystallinities of the polymers in the blended films. Therefore, we instead used the polymer lamellar diffraction peak that appeared on the q_{xy} axis. In fact, **PDBTz2** showed greater CL_L (146 Å) than **PDBTz1** (51 Å), indicating that **PDBTz2** had higher crystallinity than **PDBTz1** even in the blended film.

Charge carrier transport

To investigate the in-plane charge carrier transport properties, we fabricated organic field-effect transistor (OFET) devices with top-gate/bottom-contact (TG/BC) architectures. The polymer layer was spin-coated from a CB solution and then annealed at 200 °C for 30 min. Figure 5a–c shows the transfer and output curves of the OFET devices, respectively, and Table 4 summarizes the OFET characteristics. Both polymers showed unipolar p-channel characteristics. Interestingly, although **PDBTz2** had a face-on orientation, which is undesirable for in-plane charge carrier transport, the hole mobility ($\mu_h^{FET} = 0.198 \text{ cm}^2 \text{ V}^{-1} \text{ s}^{-1}$) was comparable to that of **PDBTz1** (0.203 cm^2 V^{-1} s^{-1}). This was probably due to

enhanced intrachain charge carrier transport in **PDBTz2**, which originated from its highly coplanar and rigid backbone. In addition, the threshold voltage (V_{th}) of **PDBTz2** (−24 V) was significantly lower than that of **PDBTz1** (−37 V), which was most likely due to its higher-lying E_{HOMO}, ensuring efficient hole injection from the electrode. The current on/off ratios (I_{on}/I_{off}) were reasonably high for both polymers (1.4×10^5 for **PDBTz1** and 1.9×10^5 for **PDBTz2**).

We also investigated the out-of-plane charge carrier transport properties with the space-charge-limited current (SCLC) model (Fig. S9 and Table S3). Although the hole-only devices for the polymer neat film did not exhibit J–V curves that fit this model, the blended films provided good J–V curves that did fit. As a result, the **PDBTz2**:Y6 blended film exhibited a hole mobility (μ_h^{SCLC}) of $1.1 \times 10^{-4} \text{ cm}^2 \text{ V}^{-1} \text{ s}^{-1}$, which was significantly greater than that of the **PDBTz1**:Y6 blended film ($3.9 \times 10^{-5} \text{ cm}^2 \text{ V}^{-1} \text{ s}^{-1}$). This most likely occurred because the crystallinity of the blended film was greater for **PDBTz2** than for **PDBTz1**, as described above. In addition, the electron mobilities (μ_e^{SCLC}) were 6–$7 \times 10^{-5} \text{ cm}^2 \text{ V}^{-1} \text{ s}^{-1}$ for both blended films. The higher μ_h^{SCLC} for the **PDBTz2**:Y6 blended relative to that for the **PDBTz1**:Y6 blended film may account for the higher J_{SC} and FF in the **PDBTz2** cell than in the **PDBTz1** cell.

Conclusions

In this work, we synthesized a new building unit in which two alkoxythiophenes were attached to BBTz, which was copolymerized with an alkylthiophene-flanked BBTz building unit. The resulting polymer, named **PDBTz2**, showed a higher HOMO energy level as well as a narrower optical bandgap than its alkyl counterpart (**PDBTz1**) owing to the electronic effects of the electron-donating alkoxy groups. The higher HOMO energy of **PDBTz2** led to a better matched energy offset of the HOMOs when blended with Y6, which facilitated charge transfer. Furthermore, with the S···O noncovalent intramolecular interactions between the alkoxy oxygens and the thiazole sulfurs in BBTz, **PDBTz2** exhibited a more coplanar and rigid backbone and greater aggregation than **PDBTz1**, resulting in greater crystallinity. Interestingly, **PDBTz2** exhibited a nearly complete face-on backbone orientation, while **PDBTz1** exhibited an edge-on orientation. As a result, the **PDBTz2**:Y6 cells exhibited remarkably higher J_{SC}s and thereby higher PCEs than the **PDBTz1**:Y6 cells. These results showed that alkoxythiophene-flanked BBTz has great potential for use as a building unit for π-conjugated polymers with highly crystalline and desirable face-on orientations. Further studies on polymers incorporating the building unit are currently underway in our group.
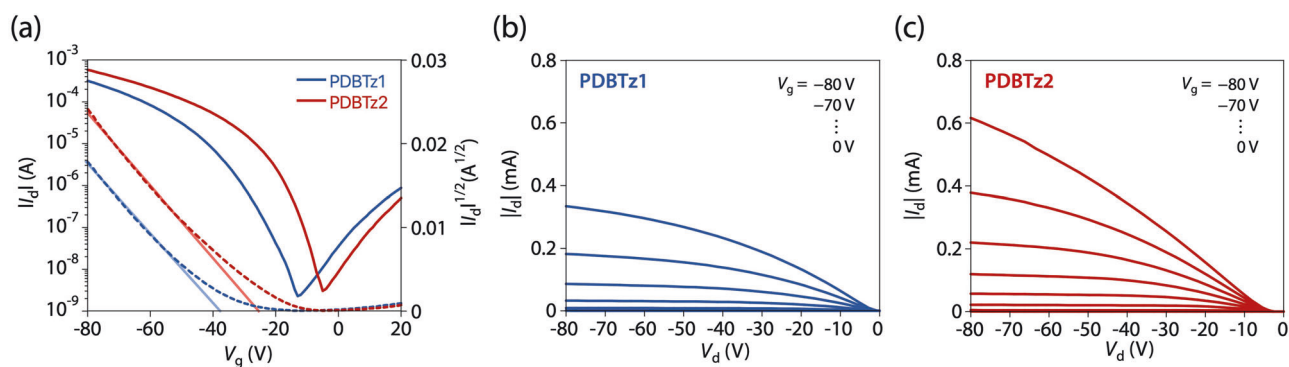
Fig. 5 a Transfer and (**b**, **c**) output curves of OFET devices of the polymers

Table 4 Charge carrier mobilities of polymers based on the FET

Polymer	μ_h^{FET} ($cm^2 V^{-1} s^{-1}$)	V_{th} (V)	I_{on}/I_{off}
PDBTz1	0.203	−37	1.4×10^5
PDBTz2	0.198	−24	1.9×10^5

Compliance with ethical standards

Conflict of interest The authors declare no competing interests.

Publisher's note Springer Nature remains neutral with regard to jurisdictional claims in published maps and institutional affiliations.

References

1. Loo Y-L, McCulloch I. Progress and challenges in commercialization of organic electronics. MRS Bull. 2008;33:653–62.
2. Inganäs O. Organic photovoltaics over three Decades. Adv Mater. 2018;30:1800388.
3. Brus VV, Lee J, Luginbuhl BR, Ko S, Bazan GC, Nguyen T. Solution-processed semitransparent organic photovoltaics: from molecular design to device performance. Adv Mater. 2019;31:1900904.
4. Yan C, Barlow S, Wang Z, Yan H, Jen AK-Y, Marder SR, et al. Non-fullerene acceptors for organic solar cells. Nat Rev Mater. 2018;3:18003.
5. Yuan J, Zhang Y, Zhou L, Zhang G, Yip H-L, Lau T-K, et al. Single-junction organic solar cell with over 15% efficiency using fused-ring acceptor with electron-deficient core. Joule. 2019;3:1140–51.
6. Jin J, Wang Q, Ma K, Shen W, Belfiore LA, Bao X et al. Recent developments of polymer solar cells with photovoltaic performance over 17%. Adv Funct Mater. 2023;33:2213324.
7. Facchetti A. π-Conjugated polymers for organic electronics and photovoltaic cell applications. Chem Mater. 2011;23:733–58.
8. Osaka I, Shimawaki M, Mori H, Doi I, Miyazaki E, Koganezawa T, et al. Synthesis, characterization, and transistor and solar cell applications of a naphthobisthiadiazole-based semiconducting polymer. J Am Chem Soc. 2012;134:3498–507.
9. Huo L, Zhang S, Guo X, Xu F, Li Y, Hou J. Replacing alkoxy groups with alkylthienyl groups: a feasible approach to improve the properties of photovoltaic polymers. Angew Chem Int Ed. 2011;50:9697–702.
10. Zhang M, Guo X, Ma W, Ade H, Hou J. A large-bandgap conjugated polymer for versatile photovoltaic applications with high performance. Adv Mater. 2015;27:4655–60.
11. Liu Q, Jiang Y, Jin K, Qin J, Xu J, Li W, et al. 18% Efficiency organic solar cells. Sci Bull. 2020;65:272–5.
12. Nakao N, Ogawa S, Kim HD, Ohkita H, Mikie T, Saito M, et al. Pronounced backbone coplanarization by π-extension in a sterically hindered conjugated polymer system leads to higher photovoltaic performance in non-fullerene solar cells. ACS Appl Mater Interfaces. 2021;13:56420–9.
13. Osaka I, Sauvé G, Zhang R, Kowalewski T, McCullough RD. Novel thiophene-thiazolothiazole copolymers for organic field-effect transistors. Adv Mater. 2007;19:4160–5.
14. Osaka I, Takimiya K, McCullough RD. Benzobisthiazole-based semiconducting copolymers showing excellent environmental stability in high-humidity air. Adv Mater. 2010;22:4993–7.
15. Osaka I, Saito M, Mori H, Koganezawa T, Takimiya K. Drastic change of molecular orientation in a thiazolothiazole copolymer by molecular-weight control and blending with PC61BM leads to high efficiencies in solar cells. Adv Mater. 2012;24:425–30.
16. Guo B, Li W, Guo X, Meng X, Ma W, Zhang M, et al. High efficiency nonfullerene polymer solar cells with thick active layer and large area. Adv Mater. 2017;29:1702291.
17. Wan P, An C, Zhang T, Ma K, Liang N, Xu Y, et al. The effect of aggregation behavior on photovoltaic performances in benzodithiophene-thiazolothiazole-based wide band-gap conjugated

polymers with side chain position changes. Polym Chem. 2019;11:1629–36.

18. Yin B, Chen Z, Pang S, Yuan X, Liu Z, Duan C, et al. The renaissance of oligothiophene-based donor–acceptor polymers in organic solar cells. Adv. Energy Mater. 2022;12:2104050.

19. Yamanaka K, Saito M, Koganezawa T, Saito H, Kim HD, Ohkita H, et al. Interplay between π-conjugated polymer donors and acceptors determines crystalline order of their blends and photovoltaic performance. Adv. Energy Mater. 2023;13:2203443.

20. Wen S, Li Y, Rath T, Li Y, Wu Y, Bao X, et al. A benzo-bis(thiazole)-based copolymer for highly efficient non-fullerene polymer solar cells. Chem Mater. 2019;31:919–26.

21. Wen S, Li Y, Zheng N, Raji IO, Yang C, Bao X. High-efficiency organic solar cells enabled by halogenation of polymers based on 2D conjugated benzobis(thiazole). J Mater Chem A. 2020;8:13671–8.

22. Nakao N, Saito M, Mikie T, Ishikawa T, Jeon J, Kim HD, et al. Halogen-free π-conjugated polymers based on thienobenzo-bisthiazole for efficient nonfullerene organic solar cells: rational design for achieving high backbone order and high solubility. Adv Sci. 2023;10:2205682.

23. Huang H, Yang L, Facchetti A, Marks TJ. Organic and polymeric semiconductors enhanced by noncovalent conformational locks. Chem Rev. 2017;117:10291–318.

24. Fei Z, Boufflet P, Wood S, Wade J, Moriarty J, Gann E, et al. Influence of backbone fluorination in regioregular poly(3-alkyl-4-fluoro)thiophenes. J Am Chem Soc. 2015;137:6866–79.

25. Cao Z, Chen J, Liu S, Jiao X, Ma S, Zhao J, et al. Synergistic effects of polymer donor backbone fluorination and nitrogenation translate into efficient non-fullerene bulk-heterojunction polymer solar cells. ACS Appl Mater Interfaces. 2020;12,:9545–54.

26. Saito M, Fukuhara T, Kamimura S, Ichikawa H, Yoshida H, Koganezawa T, et al. Impact of noncovalent sulfur–fluorine interaction position on properties, structures, and photovoltaic performance in naphthobisthiadiazole-based semiconducting polymers. Adv Energy Mater. 2020;10:1903278.

27. Guo X, Liao Q, Manley EF, Wu Z, Wang Y, Wang W, et al. Materials design via optimized intramolecular noncovalent interactions for high-performance organic semiconductors. Chem Mater. 2016;28:2449–60.

28. Chen J, Liao Q, Wang G, Yan Z, Wang H, Wang Y, et al. Enhancing polymer photovoltaic performance via optimized intramolecular ester-based noncovalent sulfur⋯oxygen interactions. Macromolecules. 2018;51:3874–85.

29. Saito M, Osaka I, Koganezawa T, Takimiya K. Effect of oxygen-containing functional side chains on the electronic properties and photovoltaic performances in a thiophene–thiazolothiazole copolymer system. Heteroat Chem. 2014;25:556–64.

30. Yamanaka K, Saito M, Mikie T, Osaka I. Effect of ester side chains on photovoltaic performance in thiophene-thiazolothiazole copolymers. Bull Chem Soc Jpn. 2021;94:2019–27.

31. Bertrandie J, Han J, Castro CSPD, Yengel E, Gorenflot J, Anthopoulos T, et al. The energy level conundrum of organic semiconductors in solar cells. Adv Mater. 2022;34:2202575.

32. Al-Naamani E, Gopal A, Ide M, Osaka I, Saeki A. Exploring alkyl chains in benzobisthiazole-naphthobisthiadiazole polymers: impact on solar-cell performance, crystalline structures, and optoelectronics. ACS Appl Mater Interfaces. 2017;9:37702–11.

33. Vezie MS, Few S, Meager I, Pieridou G, Dörling B, Ashraf RS, et al. Exploring the origin of high optical absorption in conjugated polymers. Nat Mater. 2016;15:746–53.

34. Saito M, Yamada H, Kranthiraja K, Jeon J, Kim HD, Mikie T, et al. Ordered π-conjugated polymer backbone in amorphous blend for high efficiency nonfullerene organic photovoltaics. Commun Mater. 2023;4:72.

35. Osaka I, Takimiya K. Backbone orientation in semiconducting polymers. Polymer. 2015;59:A1–15.